Asian Journal of Chemistry; Vol. 37, No. 8 (2025), 1932-1948

ASIAN JOURNAL OF CHEMISTRY

https://doi.org/10.14233/ajchem.2025.33674

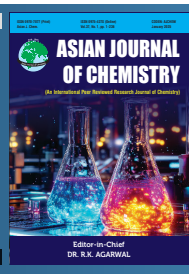

Quantum-Spectroscopic, NCI Analysis and Anticancer Studies of E and Z Conformers of Rhodocorane

JINIGI PREM CHAND, NOWDURI ANNAPURNA*, BONIGE KISHORE BABU* and CHANDAKA MANMADARAO

Department of Engineering Chemistry, AU College of Engineering (A), Andhra University, Visakhapatnam-530003, India

*Corresponding authors: E-mail: dr.bkbabu@andhrauniversity.edu.in; dr.nannapurna@andhrauniversity.edu.in

Received: 14 March 2025; *Accepted*: 5 July 2025; *Published online*: 31 July 2025; AJC-22072

In this work, theoretical methods were used to study the optimal geometries, vibrational frequencies and assignments for rhodocoranes E and Z (I & J) conformers. Time-dependent density functional theory (TD-DFT) revealed oscillator strengths and energy values aligning closely with the experiment results. Gauge-independent atomic orbital (GIAO) calculations provided ^{1}H and ^{13}C NMR chemical shifts, compared with the experimental data. The HOMO-LUMO analysis explored charge transfer, while natural bond orbital (NBO) analysis assessed stability *via* hyper-conjugation and charge delocalization. The molecular electrostatic potential (MEP) surfaces, infrared intensities and topological analyses using electron localization function (ELF) were also performed. Molecular docking studies evaluated anticancer activity against VEGFR-2 kinase inhibitors, targeting protein structures (1Y6B, 4AG8, 6GQO and 6GQP).

Keywords: Rhodotus palmatus, TD-DFT, ADMET, Molecular docking, Quantum-spectroscopic, Anticancer activity.

INTRODUCTION

Mushroom is fascinating organisms that have long captivated the attention of scientists and culinary enthusiasts alike, not just for their diverse flavours and culinary uses, but also for their rich array of bioactive metabolites [1,2]. These metabolites include polysaccharides, terpenoids, phenolic compounds, essential amino acids, vitamins and minerals, play significant roles in both nutrition and health [2,3]. Rhodocoranes, a subclass of meroterpenoids, are structurally complex natural products that have attracted significant attention in the fields of natural product chemistry, pharmacology and drug development due to their diverse bioactive properties and unique molecular structure [4,5]. These compounds, typically produced by fungi and other microorganisms, combine features of both terpenes and polyketides, making them important molecules in both chemical synthesis and medicinal research [6]. In nature, rhodocoranes and other meroterpenoids often serve protective functions for the producing organisms, acting as secondary metabolites that help in defending against predators, pathogens, or environmental stressors [7]. Their complex chemical structures and bioactivities suggest that these compounds play crucial roles in ecological interactions and their study provides insight into the chemical defences of fungi, plants and other organisms that produce them [8,9].

The structural complexity of rhodocoranes sets them apart from many other natural products. These compounds are characterized by the fusion of a sesquiterpene core with a polyketide-derived aromatic ring system, often decorated with functional groups like hydroxyl, methoxy and carbonyl groups. This unique combination of a terpene backbone with an aromatic ring contributes to the stability and reactivity of molecule, enhancing its bioactivity. The spatial arrangement of functional groups and the stereochemistry involved in rhodocorane synthesis adds an additional layer of complexity, which is often key to their biological effects [10]. The study of rhodocoranes has therefore provided valuable insights into natural product biosynthesis and the mechanisms by which microorganisms generate such diverse chemical entities.

Rhodocoranes from A-E & F-L were first isolated by Sandargo *et al*. [4,5], respectively and stereoselective rhodocoranes I and J were first synthesized by Vincent *et al.* [11], who also played a key role in determining its structure. According to a thorough review of the literature, comparative structural analysis was done with natural products isolated with that of the synthesized compounds, but no indepth quantum computational techniques were studied at for rhodocorane-I (Rh-I) and rhodocorane-J (Rh-J) compounds. This motivates the use of DFT techniques with the B3LYP/6-311G++ (d,p) level as

the basis set to offer a thorough vibrational and spectroscopic characterization (FT-IR, UV-Vis and NMR) on Rh-I and Rh-J compounds. The electrical characteristics were examined using HUMO-LUMO energies in this endeavour. Multiwfn 3.7, a wave function analysis program, provided the electron excitation and topology analysis electron localization function (ELF). Molecular electrostatic potential (MEP) and Fukui function descriptors were used to analyze the reactive sites and electron distribution. The natural bond orbitals (NBO) have also been reported. In addition to DFT calculations, mole-cular docking studies have been conducted to investigate the binding interactions of the most active molecule to the targeted proteins (VEGFR-2) inhibitors.

COMPUTATIONAL METHODS

The molecules under consideration were optimized utilizing 6-311G++(d,p) basis sets using a variety of theories, including density functional theory (DFT), MP (Møller-Plesset perturbation theory), and HF (Hartree-Fock). Even if the data from other theories revealed the comparable results, this study mostly focuses on the DFT theory findings since the DFT demonstrated more precision than the experimental evidence. Also it allows for smaller basis sets, enhances the description of polar interactions and a useful technique for conducting molecular simulations. Molecular electrostatic potential (MEP), electron localization function (ELF) and vibrational frequency were further calculated using the B3LYP/6-311G++(d,p) basis set. A number of factors crucial to this study were established using the Gaussian09 W [12] software tools, including file outputs for visualization and chart plotting, ideal geometry variables, FMO and MEP. VEDA4 [13] program was utilized for assigning the computed wavenumbers and %PED to the normal modes by using total energy distribution. The Multiwfn 3.8 software was used for topological analysis and the creation of an ELF graph [14]. The NBO3.0 program [15], which is integrated within the Gaussian09W package at the DFT/B3LYP/6-311G++(d,p) technique, was used to perform the natural bond orbital (NBO) analysis. Using the GIAO approach, the ^{1}H and ^{13}C NMR isotropic chemical shifts were computed [16,17]. The electronic parameters were computed using the TD-DFT technique and CPCM model to incorporate the solvent impact in the TD-DFT computation [18]. The density of state (DOS) spectra for the gas and methanol phases were developed using the Gauss Sum 3.0 tool [19]. Maps of the electrostatic potential surface (EPS) and reduced density gradient (RDG) are created multiwfn and VMD 9.1 program [20]. The gauge-invariant atomic orbital (GIAO) method was used to calculate the nuclear magnetic resonance (NMR) chemical shifts at the B3LYP level using the 6-311G++(d,p) basis set. The isotropic chemical shifts of ^{1}H and ^{13}C were compared to the corresponding values of TMS, which was computed at the same theoretical level. Using conductor polarizable continuum model (CPCM), the impact of solvent on the stability of the CPPS molecule and theoretical NMR parameters was taken into account. In order to compare the experimental data obtained using MeOD as the solvent, methanol was utilized. Molecular docking analysis (ligand-protein docking interactions) have been performed using Autodock Vina program 1.2.5 [21,22], along with [23] and Discovery studio visualiser v24.1.0.23298 [24].

RESULTS AND DISCUSSION

Molecular geometry: According to the provided atom numbering scheme, the optimized geometrical parameters of conformers of rhodocorane I and J were determined using the B3LYP level with the 6-311G++(d,p) basis set and optimized parameters of I are given in Table-1, which are in accordance with the atom numbers. It is observed that bond lengths and bond angles of both the conformers were almost same with a correlation coefficient of 0.9999 and 0.9946 for bond lengths and bond angles, respectively (Fig. 1a-b) and they are unaltered by the ring flip. There are discrepancies in the dihedral angles as 2-furanone moiety was flipped by 1800. Due to the unavailability of the exact crystal structures, the results weren't compared with the experimental values.

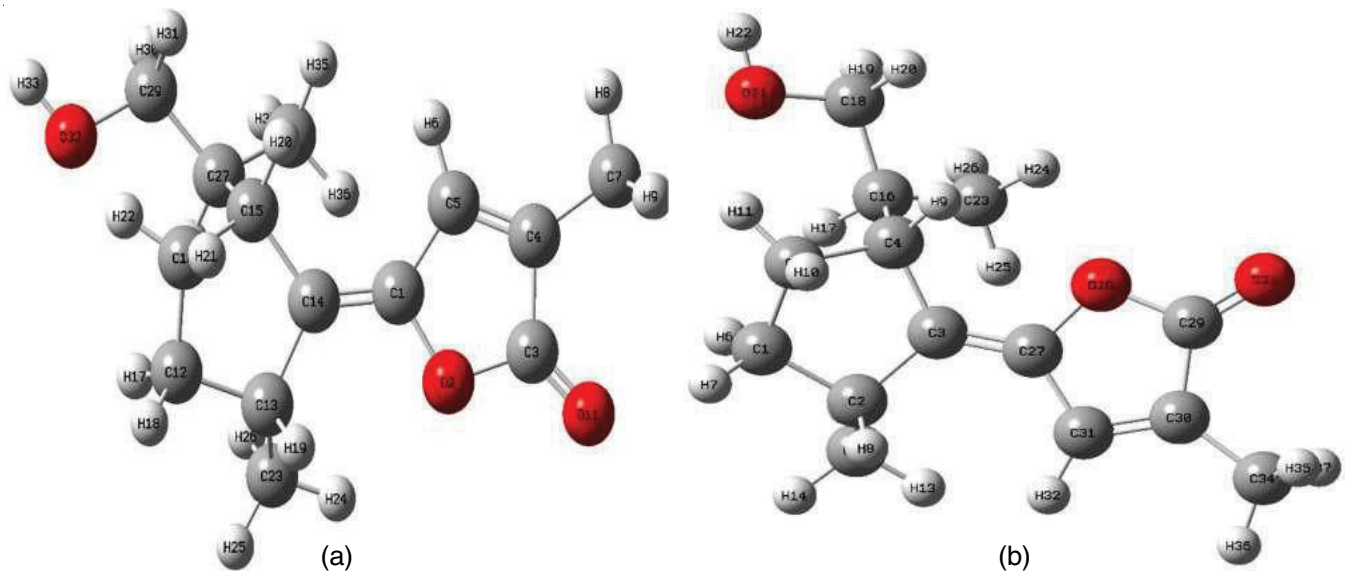

Fig. 1. Stable conformers (a) rhodocorane I and (b) rhodocorane J

TABLE-1
MOLECULAR STRUCTURE PARAMETERS OF RHODOCORANE I

Atoms bonded	Bond length	Atoms bonded	Bond angle	Atoms bonded	Dihedral angle	2nd Angle type
C5–C4	1.3490	C1–C5–C4	109.2408	C3–C4–C5–C1	0.0662	Dihedral
C1–C5	1.4484	C3–C4–C5	107.0532	O2–C1–C5–C4	0.0515	Dihedral
C3–C4	1.4792	O2–C1–C5	107.518	C14–C1–O2–C5	132.124	Pro-R
O2–C1	1.3935	C14–C1–O2	120.3363	C13–C14–C1–O2	4.7072	Dihedral
C14–C1	1.3431	C13–C14–C1	123.6423	C15–C14–C13–C1	125.418	Pro-R
C13–C14	1.5236	C15–C14–C13	110.3921	C12–C13–C14–C15	-8.8962	Dihedral
C15–C14	1.5188	C12–C13–C14	103.7507	C16–C15–C14–C13	30.3506	Dihedral
C12–C13	1.5514	C16–C15–C14	100.3106	H6–C5–C1–C4	126.9118	Pro-R
C16–C15	1.5516	H6–C5–C1	123.8456	C7–C4–C3–C5	130.8828	Pro-S
H6–C5	1.0801	C7–C4–C3	122.0617	C23–C13–C12–C14	114.6766	Pro-R
C7–C4	1.4908	C23–C13–C12	113.8612	C27–C15–C14–C16	113.9406	Pro-R
C23–C13	1.5377	C27–C15–C14	113.3697	O11–C3–O2–C4	130.3769	Pro-S
C27–C15	1.5638	O11–C3–O2	122.1344	H17–C12–C13–C16	109.8996	Pro-S
O11–C3	1.2018	H17–C12–C13	110.1295	H18–C12–C13–C16	112.6167	Pro-R
H17–C12	1.0944	H18–C12–C13	112.0523	H19–C13–C12–C14	107.3702	Pro-S
H18–C12	1.0923	H19–C13–C12	109.5739	H20–C15–C14–C16	110.9838	Pro-S
H19–C13	1.0961	H20–C15–C14	111.2277	H21–C16–C12–C15	108.421	Pro-R
H20–C15	1.0958	H21–C16–C12	109.8927	H22–C16–C12–C15	113.199	Pro-S
H21–C16	1.0955	H22–C16–C12	112.9048	C29–C27–C15–C14	174.8831	Dihedral
H22–C16	1.0882	C29–C27–C15	112.5205	C34–C27–C15–C29	108.7226	Pro-S
C29–C27	1.5354	C34–C27–C15	111.8405	H28–C27–C15–C29	106.3945	Pro-R
C34–C27	1.5359	H28–C27–C15	108.9271	O32–C29–C27–C15	-81.1231	Dihedral
H28–C27	1.0952	O32–C29–C27	110.1803	H30–C29–C27–O32	109.4914	Pro-R
O32–C29	1.4325	H30–C29–C27	108.8578	H31–C29–C27–O32	110.5512	Pro-S
H30–C29	1.0968	H31–C29–C27	110.0123	H8–C7–C4–C3	-179.5515	Dihedral
H31–C29	1.1002	H8–C7–C4	111.3173	H9–C7–C4–H8	108.6898	Pro-S
H8–C7	1.0913	H9–C7–C4	110.7131	H10–C7–C4–H8	108.6919	Pro-R
H9–C7	1.0941	H10–C7–C4	110.7282	H24–C23–C13–C12	-178.4116	Dihedral
H10–C7	1.0942	H24–C23–C13	111.1936	H25–C23–C13–H24	108.1629	Pro-S
H24–C23	1.0912	H25–C23–C13	110.0391	H26–C23–C13–H24	108.453	Pro-R
H25–C23	1.0942	H26–C23–C13	111.0952	H33–O32–C29–C27	-175.75	Dihedral
H26–C23	1.0942	H33–O32–C29	108.7659	H35–C34–C27–C15	-65.1957	Dihedral
H33–O32	0.962	H35–C34–C27	111.3083	H36–C34–C27–H35	107.7878	Pro-S
H35–C34	1.0963	H36–C34–C27	111.6415	H37–C34–C27–H35	107.4834	Pro-R
H36–C34	1.0903	H37–C34–C27	110.6611	–	–	–
H37–C34	1.0934	–	–	–	–	–

Vibrational analysis: Each of the 37 atoms in the title conformers has 105 normal vibration modes and is a member of the C1 point group. There are 105 modes of vibration, of which 35 are stretching modes, 36 are bending modes and 34 are torsional modes. In order to remove errors from the harmonic wavenumber output, a uniform scaling procedure was used in this work. In the range of 3200 to 1700 cm^{-1} and below 1700 cm^{-1}, the theoretical harmonic wavenumbers have been scaled by a factor of 0.958 and 0.983, respectively [25]. Table-2 summarizes the detailed assignments and the PED percentage; assignments with a PED percentage of less than 10% are disregarded.

O-H vibrations: For an isolated O-H group, the stretching frequency comes around 3610-3640 cm^{-1}, experimentally. The scaled stretching value for the heteroatomic molecule rhodocorane was 3679 cm^{-1}, which is a pure stretching contributes 100% as shown by PED. Also, O-H shows a deformation vibration at 260 cm^{-1} (mode 72). In plane vibrations, O-H, were assigned at 1422, 1239, 1088 cm^{-1}. Furthermore, the mixed assignments were done for O-H out-of-plane bending vibrations and C-OC and C-C-O bending vibrations in 494 cm^{-1} and 260 cm^{-1}, respectively.

C=O vibrations: Computational calculations of C=O vibrations are a powerful tool to predict, analyze and correlate vibrational characteristics with structural and electronic properties of carbonyl-containing compounds. Due to significant difference between the dipole moment of C and O, C=O stretching vibrations appear at 1800-1650 cm^{-1}. But frequency of C=O in five membered cyclic esters appear from 1750 cm^{-1}. It was observed that in the computed values, 1742 cm^{-1} with 87% of PED. The increase in frequency of the carbonyl (from the base value of 1715 cm^{-1} for free carbonyl) is attributed to the electron withdrawing group -OR and its conjugation within the furanone ring.

C-O vibrations: In the titled compound, there are three different C-O groups are present, one is the C-O present in conjugated ester, second is conjugated C-O within the furanone and the other is aliphatic alcohol attached carbon. The first gives two or more peaks around 1300-1000 cm^{-1}, in this analysis we obtained 748 cm^{-1}, it is due to the conjugation within ring. For C-O within the furanone, 968 and 816 cm^{-1} were obtained, whereas the alcoholic bonded to C-O, a value of 1020 cm^{-1} was calculated. All these values show good agreement with experimental knowledge.

TABLE-2
VIBRATIONAL FREQUENCY ASSIGNMENTS OF RHODOCORANE-I
CALCULATED WITH B3LYP METHOD USING 6-311G++(d,p) BASIS SET

Normal mode No.	Frequency scaled	IR	Assignment (% PED)
1	3679.8	43.0	νO32–H33 (100)
2	3093.4	2.8	νC5–H6 (99)
3	2998.1	7.6	νC16–H22 (95)
4	2985.6	18.0	νC29–H30 (76)
5	2980.9	13.4	νC7–H8 (93)
6	2980.4	14.6	νC23–H25 (17)
7	2955.3	75.3	νC12–H17 (81)
8	2951.5	5.9	νC12–H17 (90)
9	2949.3	41.0	νC29–H30 (78)
10	2948.7	7.9	νC7–H9 (100)
11	2917.5	61.6	νC15–H20 (13)
12	2909.4	16.4	νC12–H17 (79)
13	2903.7	20.3	νC15–H20 (13)
14	2902.4	22.8	νC7–H8 (93)
15	2896.6	31.2	νC23–H25 (17)
16	2891.2	52.0	νC15–H20 (72)
17	2890.5	1.6	νC13–H19 (81)
18	2888.9	8.9	νC13–H19 (80)
19	2885.5	23.5	νC29–H30 (72)
20	2845.9	42.3	νC29–H30 (85)
21	1742.8	794.8	νO11–C3 (87)
22	1640.2	10.1	νC14–C1 (73)
23	1631.0	21.1	νC4–C5 (73)
24	1493.5	8.1	βH30C29H31 (59)
25	1487.0	7.1	βH17C12H18 (60)
26	1484.0	3.4	βH24C23H25 (11) + βH24C23H25 (61)
27	1478.4	7.7	βH24C23H25 (11) + βH24C23H25 (61)
28	1475.0	2.8	βH35C34H36 (68)
29	1469.3	7.6	βH17C12H18 (76)
30	1467.4	3.4	βH21C16H22 (73)
31	1461.1	7.1	βH8C7H10 (69) + βH8C7H10 (12)
32	1448.9	7.9	βH8C7H10 (83) + βH8C7H10 (15)
33	1422.5	5.2	βH33O32C29 (19) + βH33O32C29 (17) + βH33O32C29 (35) + βH33O32C29 (11)
34	1395.6	2.0	βH8C7H10 (93)
35	1388.0	5.4	βH35C34H36 (91)
36	1380.4	3.6	βH24C23H25 (91)
37	1353.0	0.2	νC27–C15 (14)
38	1333.5	9.7	τH21–C16–C15–C27 (31) + τH21–C16–C15–C27 + τH21–C16–C15–C27
39	1324.1	2.8	βH18C12C16 (11) + βH18C12C16 (20) + βH18C12C16 (20)
40	1317.0	0.5	βH6C5C4 (12) + βH6C5C4 (15) + βH6C5C4 (18) + βH6C5C4 (11)
41	1306.8	9.5	βH28C27C34 (16) + βH28C27C34 (26)
42	1303.3	7.8	βH19C13C23 (13) + βH19C13C23 (26)
43	1294.1	0.5	τH19–C13–C14–C15 (42) + τH19–C13–C14–C15 + τH19–C13–C14–C15
44	1287.2	1.9	βH20C15C14 (14) + βH20C15C14 (32)
45	1262.7	38.6	νC1–C5 (22)
46	1258.7	5.5	βH18C12C16 (11) + βH18C12C16 (20) + βH18C12C16 (20)
47	1239.9	18.6	βH33O32C29 (19) + βH33O32C29 (17) + βH33O32C29 (35) + βH33O32C29 (11)
48	1225.8	33.2	βH33O32C29 (19) + βH33O32C29 (17) + βH33O32C29 (35) + βH33O32C29 (11)
49	1204.0	1.7	βH20C15C14 (14) + βH20C15C14 (32)
50	1192.7	0.3	νC4–C7 (11)
51	1181.0	10.3	βH18C12C16 (11) + βH18C12C16 (20) + βH18C12C16 (20)
52	1154.6	9.4	νC13–C14 (16)
53	1125.8	6.9	γC23–C12–C14–C13 (15) + γC23–C12–C14–C13 (14)
54	1107.8	9.0	νC16–C12 (15)
55	1088.8	8.6	βH33O32C29 (19) + βH33O32C29 (17) + βH33O32C29 (35) + βH33O32C29 (11)
56	1083.4	8.3	νC23–C13 (31)

57	1043.5	1.0	βH8C7H10 (83) + βH8C7H10 (15)
58	1040.2	87.9	νC1–C5 (40)
59	1036.5	9.9	βH18C12C16 (23) + βH18C12C16 (11)
60	1020.8	52.8	νC12–C16 (33)
61	1020.4	67.8	νO32–C29 (30)
62	998.9	2.2	νC16–C12 (28)
63	989.3	90.9	βH6C5C4 (12) + βH6C5C4 (15) + βH6C5C4 (18) + βH6C5C4 (11)
64	968.3	74.3	νO2–C1 (13)
65	951.6	2.8	τH18–C12–C16–C15 (15) + τH18–C12–C16–C15 (20) + τH18–C12–C16–C15 (12)
66	936.3	7.6	νC16–C12 (15)
67	922.3	0.2	νC16–C12 (28)
68	891.4	5.8	νC23–C13 (31)
69	880.0	15.5	τH6–C5–C4–C7 (39) + τH6–C5–C4–C7 (32)
70	875.0	5.9	τH6–C5–C4–C7 (39) + τH6–C5–C4–C7 (32)
71	852.0	2.5	Ring group bending (34)
72	816.9	4.0	νO2–C1 (13)
73	800.8	3.1	νC27–C15 (14)
74	790.9	1.0	νC4–C7 (11)
75	748.0	11.6	γO11–C4–O2–C3 (64)
76	725.5	2.4	Ring group bending (41)
77	677.2	1.5	τC1–C14–C13–C12 (19)
78	612.7	12.0	νC4–C7 (11)
79	599.5	1.1	βC12C13C14 (19)
80	586.4	2.9	βO2C3O11 (39) + βO2C3O11 (10)
81	548.2	3.5	τC3–O2–C1–C5 (12) + τC3–O2–C1–C5 (35)
82	494.4	2.6	βO32C29C27 (14) + βO32C29C27 (13) + βO32C29C27 (20)
83	446.3	6.4	βO2C3O11 (39) + βO2C3O11 (10)
84	407.6	0.1	βC5C4C7 (13) + βC5C4C7 (11) + βC5C4C7 (19) + βC5C4C7 (25)
85	399.7	2.6	γC23–C12–C14–C13 (15) + γC23–C12–C14–C13 (14)
86	365.9	0.1	γC7–C3–C5–C4 (27)
87	353.4	0.4	γC15–C13–C1–C14 (17)
88	338.3	5.1	βC12C13C23 (10) + βC12C13C23 (20)
89	283.3	2.5	βC5C4C7 (51)
90	263.0	7.0	τH35–C34–C27–C15 (41) + τH35–C34–C27–C15 (24)
91	260.2	91.5	τH33–O32–C29–C27 (81)
92	253.0	3.6	βC23C13C12 (19)
93	244.6	3.3	βC5C4C7 (13) + βC5C4C7 (11) + βC5C4C7 (19) + βC5C4C7 (25)
94	234.4	2.0	βC5C4C7 (13) + βC5C4C7 (11) + βC5C4C7 (19) + βC5C4C7 (25)
95	218.5	0.9	βC5C4C7 (13) + βC5C4C7 (11) + βC5C4C7 (19) + βC5C4C7 (25)
96	215.8	8.2	βC15C27C29 (10)
97	165.4	0.5	γC27–C14–C16–C15 (11) + γC27–C14–C16–C15 (45)
98	144.8	1.2	βC1C14C13 (11)
99	117.4	0.0	τH8–C7–C4–C3 (14) + τH8–C7–C4–C3 (36)
100	113.4	9.5	τH30–C29–C27–C15 (12) + τH30–C29–C27–C15 (11) + τH30–C29–C27–C15 (14)
101	94.3	0.6	βC1C14C13 (60)
102	79.8	0.8	γC7–C3–C5–C4 (69)
103	65.0	3.0	γC14–C5–O2–C1 (63)
104	50.1	0.3	γC14–C5–O2–C1 (63)
105	23.8	0.7	τC16–C15–C27–C29 (80)

Furanone ring vibrations: Furanone ring C-C stretching vibrations occur in the 1600-1300 cm^{-1} region and the replacement nature has no apparent influence on it. Stretching modes at 1262 and 1040 cm^{-1} corresponds to the C-C vibrations. The furan analogues generally present moderate to strong bands between 1680-1560 cm^{-1}, 1520-1470 cm^{-1} and 1400-1390 cm^{-1}, which are due to the ring stretching vibration of the C=C. This compound shows 1631 and 1640 cm^{-1} for the aromatic C=C stretching vibrations with both having %PED 73, which shows that these are pure modes of vibrations. The bending and out of plane vibrations of O-C-O fragment are assigned to 548 and 446 cm^{-1}.

CH_2 vibrations: Spectral studies show normally the asymmetric stretching vibrations for CH_2 (methylene) group falls around 3000-2900 cm^{-1}, while CH_2 (methylene) symmetric stretching vibrations appear between 2900-2800 cm^{-1} [26]. The computed values at B3LYP/6-311G++(d,p) level show that C12-H2, C16-H2 and C29-H2 the C-H symmetrical vibrations

appear at 2951, 2909, 2998, 2985, 2949 and 2845 cm^{-1} with PED % ranging between 76 to 90. It is well known that the CH_2 bending vibrations are found between 1450-875 cm^{-1}. In this analysis, we observed that 1487, 1467, 1493 cm^{-1} corresponds to the CH_2 scissoring vibrations.

CH_3 vibrations: The molecule under consideration process are the three methyl groups C23H3, C7H3 and C34H3. The C-H stretching vibration in CH_3 occurs at lower frequencies than those of aromatic ring (3100-3000 cm^{-1}). The computed values at B3LYP/6-311G++(d,p) level assigned that 2902 and 2896 cm^{-1} corresponds to the C-H symmetric vibrations and 2980, 2948 cm^{-1} were assigned to asymmetric vibrations with more than 90% PED. 1484,1478 and 1461 cm^{-1} were assigned to in plane vibrations of scissoring. Whereas 1380, 1395, 1388, 1306 cm^{-1} were assigned to the deformation vibrations in out of plane wagging. The frequencies at 1448, 1475 cm^{-1} were attributed to twisting vibrations.

CH vibrations: In this molecule, there are only four C-H moieties, C5-H6, C15-H20, C13-H19 and C27-H28. Among these H6 is a aromatic proton and C5-H6 appears at 3093 cm^{-1} with 99% PED. The other two C-H vibrations came out to be at 2917 and 2890 cm^{-1} with 13% and 81%, respectively. The last C-H is coupled with the neighbouring methyl group and it stretches asymmetrically at 1306 cm^{-1}. The C-H out-of-plane bending vibrations seem to be strongly coupled with other vibrations and appear in the range of 1000-750 cm^{-1}. The out of plan bending vibrations are assigned to 989, 1287, 1303 cm^{-1} for the corresponding C-H vibrations.

Other vibrations: With changes in the dihedral angle, the torsional vibrations become more pronounced. In this case, neither bond angles nor bond lengths are changed. The spatial relationship between the atoms affixed to each of the two adjacent atoms has changed, though. The Rh-I molecule's torsional vibration frequencies have been determined. The calculated values for the in-plane HCCC vibrations are 1333 and 1294, 951, 880 cm^{-1}. The inplane COCC vibrations computed values are at 548 with low PED% of 35. The vibration HOCC obtained a value of 260 cm^{-1} with good amount of contribution (81%) to the PED. The out of plane torsional vibrations of OCOC, have shown a value of 748 cm^{-1} with 64% PED.

NMR: NMR chemical shifts plays crucial role in identifying the structure, functional groups and indicates the conformational preferences of the molecules. Reliable calculations of magnetic properties rely upon accurate predictions of molecule geometries. Therefore, the conformers (Rh-I and Rh-J) were optimized by using B3LYP/6-311G++(d,p) method and GIAO ^1H and ^{13}C chemical shift calculations were performed by the same method. The computed chemical shift values for the ^1H and ^{13}C are summarized in Table-3. Experimental values [11] are compared with the calculated chemical shifts and from the regression analysis it is concluded that ^{13}C chemical shifts are in full agreement as summarized in Table-3. It also signifies that B3LYP/6-311G++(d,p) method is better method for the analysis of Rh-I and Rh-J conformers.

The GIAO or gauge-invariant atomic orbital method, is a powerful computational technique used in NMR spectral analysis to calculate the magnetic shielding tensors for molecular systems. By applying a gauge-invariant approach, GIAO effectively accounts for the effects of external magnetic fields on the electronic structure of molecules, which is crucial for accurate NMR predictions. This method allows for the calculation of chemical shifts and spin-spin coupling constants with high precision, facilitating the interpretation of NMR spectra. Its incorporation into quantum chemical calculations enables the researchers to gain deeper insights into molecular interactions and conformational dynamics, making it an essential tool in modern spectroscopic studies. The predicted NMR chemical shifts for the title compound derived from the B3LYP/6-311G ++(d,p) method, alongside the experimental NMR [5] chemical shifts for comparison in Table-4. ^{13}C NMR values are computed with shielding constant 182.466 and scaled with the same level of theory with TMS as reference.

TABLE-3
CORRELATION COEFFICIENTS OF THE CALCULATED *vs.* EXPERIMENTAL NMR CHEMICAL SHIFT VALUES OF Rh-I AND Rh-J

R^2 (Cal *vs.* Exp)	Rhodocorane-I	Rhodocorane-J
^1H	0.9532	0.9596
^{13}C	0.9963	0.9956

Absorption spectra: The electronic spectra of rhodocoranes I & J were computed for both the gas phase and a methanol environment. It showed Z conformer (R-J) have red shift when compared to that of the E conformer (R-I), which correlated well with that of the reported experimental values reported by Sandargo *et al.* [5] and are summarized in Table-5. The solvent effect was assessed using the PCM-TD-DFT method. The results indicate that the transition from the HOMO (highest occupied molecular orbital) to the LUMO (lowest unoccupied molecular orbital) corresponds to the maximum absorption band in the UV-vis spectrum. The slight differences in absorption wavelengths between solvent and gas phase indicate that these solvents had little to no effect on the optical properties of the molecule. In the gas phase calculations, the HOMO is identified as molecular orbital number 64 with 'A' symmetry, while the LUMO is molecular orbital number 65, also with 'A' symmetry. The first allowed dipole transition (64A→ 65A) in the gas phase has a very low oscillation strength of 0.6903, followed by another transition (63→65) with an even lower oscillation strength of 0.6866. Another significant transition is from (62→65) with the oscillator strength of 0.6888.

In comparison to the gas phase results, the transition (64A →65A) in the methanol environment exhibits an oscillation strength of 0.6908, while the transition (63→65) shows a lower oscillation strength of 0.009. The experimental absorption spectrum reveals two peaks at 295, 200, which are associated with n-π* and π→π* transitions. The observed red shift of the computed maximum compared to the experimental values can be attributed to charge transfer interactions. When R-I and R-J absorbance spectra were compared, bathochromic shift was observed due to the *trans*-isomers typically absorb at shorter wavelengths compared to *cis*-isomers. Because of the greater symmetry in *trans* isomers, which results in the higher energy requirements for electronic transitions.

TABLE-4
EXPERIMENTAL AND THEORETICAL ^{1}H NMR ISOTROPIC CHEMICAL SHIFTS (ppm, WITH RESPECT TO TMS AND IN MeOH SOLUTION) OF RHODOCORANE I & J (ATOM POSITIONS WERE NUMBERED AS IN Fig. 1)

No.	Atoms	Rh-I-^{1}H			Rh-J-^{1}H		
		^{1}H Gas	^{1}H MeOH	Expt	^{1}H Gas	^{1}H MeOH	NMR-MeOD-EXPT-^{1}H
1	C1	151.6161	150.6923	145.6	150.8367	149.9581	144.9
2	O2	265.9978	264.9541	–	270.1015	269.8519	–
3	C3	173.9337	177.2815	173.3	173.4362	176.7698	173.1
4	C4	133.9903	132.6706	128.5	135.0291	133.6936	128.4
5	C5	139.6888	143.238	138.3	138.403	141.8547	137.5
6	H6	6.922	7.3447	7.47	7.1063	7.5113	7.52
7	C7	12.3317	11.5355	10.6	12.474	11.7049	10.4
8	H8	1.6986	1.9807	1.97	1.927575	1.88115	1.96
9	H9	1.923075	1.86115	1.97	1.7632	2.03375	1.96
10	H10	1.923075	1.86115	1.97	1.927575	1.88115	1.96
11	O11	394.6288	348.5086	–	392.4496	347.1152	–
12	C12	33.823	33.535	33.2	34.6952	34.259	33.5
13	C13	42.5347	42.9052	38.1	41.1327	41.4708	37.5
14	C14	148.8375	153.9177	139.4	149.0938	154.4276	139.2
15	C15	56.227	56.2421	46.1	55.8287	56.309	46.1
16	C16	33.1523	32.9764	30.6	33.8146	33.685	28.6
17	H17	1.601	1.54475	1.5	1.51795	1.55645	1.55
18	H18	1.923075	1.9807	2	1.927575	2.03375	1.92
19	H19	3.12755	3.1104	3.06	2.8232	3.03795	3.04
20	H20	2.1565	2.4574	2.76	2.9555	2.9101	2.95
21	H21	1.4649	1.54475	1.7	1.51795	1.55645	1.74
22	H22	3.12755	3.0593	1.96	3.2016	3.03795	1.92
23	C23	21.5496	21.1665	21.1	24.2932	23.877	22.8
24	H24	1.923075	1.7206	1.26	1.1721	1.2598	1.19
25	H25	1.1721	1.2279	1.26	1.2637	1.3202	1.19
26	H26	0.7145	0.8602	1.26	0.97625	1.0142	1.19
27	C27	40.6219	40.7012	39.6	41.4511	41.3601	39.1
28	H28	1.7753	1.7206	1.72	1.927575	1.9564	2.15
29	C29	74.3434	74.2144	66.3	76.7829	76.7942	66.2
30	H30	3.7336	3.8208	3.64	3.8914	3.9736	3.61
31	H31	3.6093	3.7591	3.49	3.7849	3.828	3.39
32	O32	35.1257	29.6252	–	34.2333	29.1619	–
33	H33	0.0133	0.6458	–	0.0759	0.776133	–
34	C34	18.2086	17.547	17.3	17.037	16.8855	16.7
35	H35	0.2932	0.5132	0.95	0.97625	0.776133	1.01
36	H36	1.0049	0.8602	0.95	0.8362	0.776133	1.01
37	H37	0.7145	0.7793	0.95	0.5184	0.641800	1.01

TABLE-5
CALCULATED OSCILLATOR STRENGTH AND ASSIGNMENTS OF COMPOUNDS Rh-I AND Rh-J

B3LYP/6-311G++(d,p) In gas phase		B3LYP/6-311G++(d,p) In MeOH solvent phase		Exp. (nm)	In solvent major contribution (10%)
Wavelength (nm)	Osc. strength (f)	Wavelength (nm)	Osc. strength (f)		
Rhodocorane-I					
292.7193	0.5513	300.3493	0.6908	295	HOMO->LUMO (98%)
282.6495	0.0175	262.5115	0.0011		H-2->LUMO (92%)
236.3314	0.0018	247.1724	0.009		H-1->LUMO (95%)
233.9369	0.0106	229.9879	0.021	200	H-3->LUMO (94%)
228.0672	0.0147	225.5898	0.0054		HOMO->L+1 (87%)
227.0731	0.0188	219.2780	0.003		H-4->LUMO (87%)
Rhodocorane-J					
295.1442416	0.536	302.245662	0.6723	296	HOMO->LUMO (98%)
283.463712	0.0147	263.3982559	0.0021		H-2->LUMO (97%)
241.2566267	0.0042	247.1478551	0.0078		H-1->LUMO (99%)
234.5741992	0.0025	231.4130933	0.0332	202	H-3->LUMO (96%)
228.5170175	0.05	225.7829531	0.0026		HOMO->L+1 (90%)
223.681093	0.0002	220.9269298	0.0038		H-4->LUMO (85%)

The frontier orbitals (HOMO and LUMO) play a crucial role in quantum science, influencing a compound's interactions with other molecules, its reactivity and its kinetic stability. The small gap between these frontier molecular orbitals indicates that the compound is highly polarized, reactive and kinetically unstable or soft. These parameters, which are determined by frontier molecular orbital (FMO) energies, provide insights into various areas of pharmacological research, including drug development and potential ecotoxicological effects. Fig. 2 presents the calculated FMO values at the specified level, along with several factors influencing chemical stability and reactivity. The highest occupied molecular orbital (HOMO) energy of -6.3329 eV indicates the strength of the electron binding within the molecule; a more negative HOMO value signifies greater electron stability. In contrast, the lowest unoccupied molecular orbital (LUMO) has an energy of -2.0435 eV and its relatively low value suggests that electrons can more easily transition into this orbital. Table-6 illustrates the chemical stability of compound, showing a high chemical hardness of 2.1447 and a low chemical softness [27] of 0.4663, which indicate the non-toxicity. The title compound has sufficiently high electrophilicity index (2.39) and hence deemed to be biologically active [28]. The electron affinity of molecule is reflected in its electronegativity value of 4.1882. Both HOMO and LUMO levels reveal a balanced distribution of positive and negative phases throughout the molecule.

TABLE-6
CALCULATED ENERGY VALUES OF THE E AND Z CONFORMERS OF RHODOCORANE AT B3LYP/6 311++G(d,p)

	Rh-I	Rh-J
Ionization potential (IE) = –E(HOMO)	6.3329	6.3345
Electron affinity (EA) = –E(LUMO)	2.0435	2.0727
Chemical hardness (η) = ½ (IE–EA)	2.1446	2.1309
Chemical softness (S) = 1/η	0.4663	0.4693
Chemical potential (μ) = –0.5 (IE + EA)	-4.1882	-4.2036
Electronegativity (χ) = –μ	4.1882	4.2036
Electrophilicity index ω = $\mu^2/2\eta$	4.0895	4.14618

Molecular electrostatic potential (MEP): The electrostatic potential (ESP) is a method used to investigate the molecular characteristics and intermolecular associations of small molecules, the biological function of haemoglobin and enzyme catalysis, the activities of pharmacological compounds and their analogues [29]. Since it shows the most likely regions for the electrophilic attack of charged point-like reagents on organic compounds, ESP is widely employed. The positive electrostatic potential is associated with the repulsion of the proton by atomic nuclei in areas where low electron density exists and the nuclear charge is not fully shielded, whereas the negative electrostatic potential is associated with the attraction of the proton by the concentrated electron density in the molecule Fig. 3 displays the overall density plot and its array for Rh-I. The Rh-I molecule's ESP and its array, respectively. The chemically active locations and relative reactivity of atoms are shown visually in these illustrations. The ESP plot indicates that the molecule contains both positive and zero potential areas.

Density of states: In the boundary region, neighbouring orbitals may exhibit quasi-degenerate energy levels, meaning that HOMO and LUMO alone may not adequately describe the frontier molecular orbitals. To address this, total density of states (TDOS), partial density of states (PDOS) and bond order populations (COOP) were analyzed using Mulliken population analysis and Gaussian curves of unit height and full width at half maximum. These analyses provide a visual representation of the molecular orbital composition and associated information. A notable feature of the density of states (DOS) plot is its ability to reveal the contribution of molecular orbitals to chemical bonding through the COOP spectrum. This spectrum clearly differentiates between bonding, antibonding and non-bonding interactions. The positive values in the OPDOS plot indicate bonding interactions, whereas the negative values indicate antibonding interactions and a value of zero represents non-bonding interactions. The HOMO orbitals are primarily localized over the C=C bond, contributing 67%, while the LUMO has a contribution of 79%. The graphical representations of TDOS and PDOS are shown in Fig. 4.

NBO analysis: Estimating the distribution of electron density and atom-to-atom bonds is done using the localized orbitals. For chemical interpretation of electron density transfer (EDT) and hyper conjugative interactions, NBO analysis is a very useful tool. The intensity of the interaction between electron donors and electron acceptors increases with increasing E(2) values. Delocalization of electron density between occupied Lewis-type NBO orbitals (bond or lone pair) and formally unoccupied non-Lewis NBO orbitals (anti-bond or Rydberg) is equivalent to stabilizing the donor-acceptor interaction. NBO analysis was performed on the title molecule using the B3LYP/6-311G++(d,p) Pop=NBO test basis set in order to understand the intermolecular hydrogen bonding, intermolecular charge transfer (ICT), hybridization and delocalization of electron density. The corresponding results of second order perturbation theory analysis of fock matrix are given in Table-7.

From the results, it is obvious that the intramolecular interactions are due to the orbital overlap of the studied molecule rhodocorane-I, a very strong interaction has been observed between the bond pair electrons in donor acceptor moieties. The delocalization in furanone ring is evident that donor to acceptor moieties with higher stabilization energies lone pair of O2 to π*(C3-O11), π(C3-O11) to π*(C4-C5), π(C4-C5) to π*(C1-C14), with higher stabilization energies of 36.36, 69.49 and 59 kcal/mol. Likewise, a very strong interaction has been observed between π(C4-C5) to π*(C3-O11) and π*(C1- O14) with stabilization energies of 21.49 and 16.27 kcal/mol. Also, a significant amount of interaction is observed σ(C27-C34) over σ*(C12-C16), σ*(C34-H36), σ*(C34-H37) with stabilization energies of 10.21, 13.01, 32.05 kcal/mol. An interaction has been observed due to electron density from LP(2) of O11 to anti bonding orbitals of O2-C3 and C3-C4 with stabilization energies 36.39 and 17.11 kcal/mol.

The bonding nature of the molecular system is described by the obtained NBO results (Table-8). For instance, Table-7 shows that LP2(O11) occupies a higher energy (0.0008 a.u.) with a major p-character (99.90%) and a low occupation number

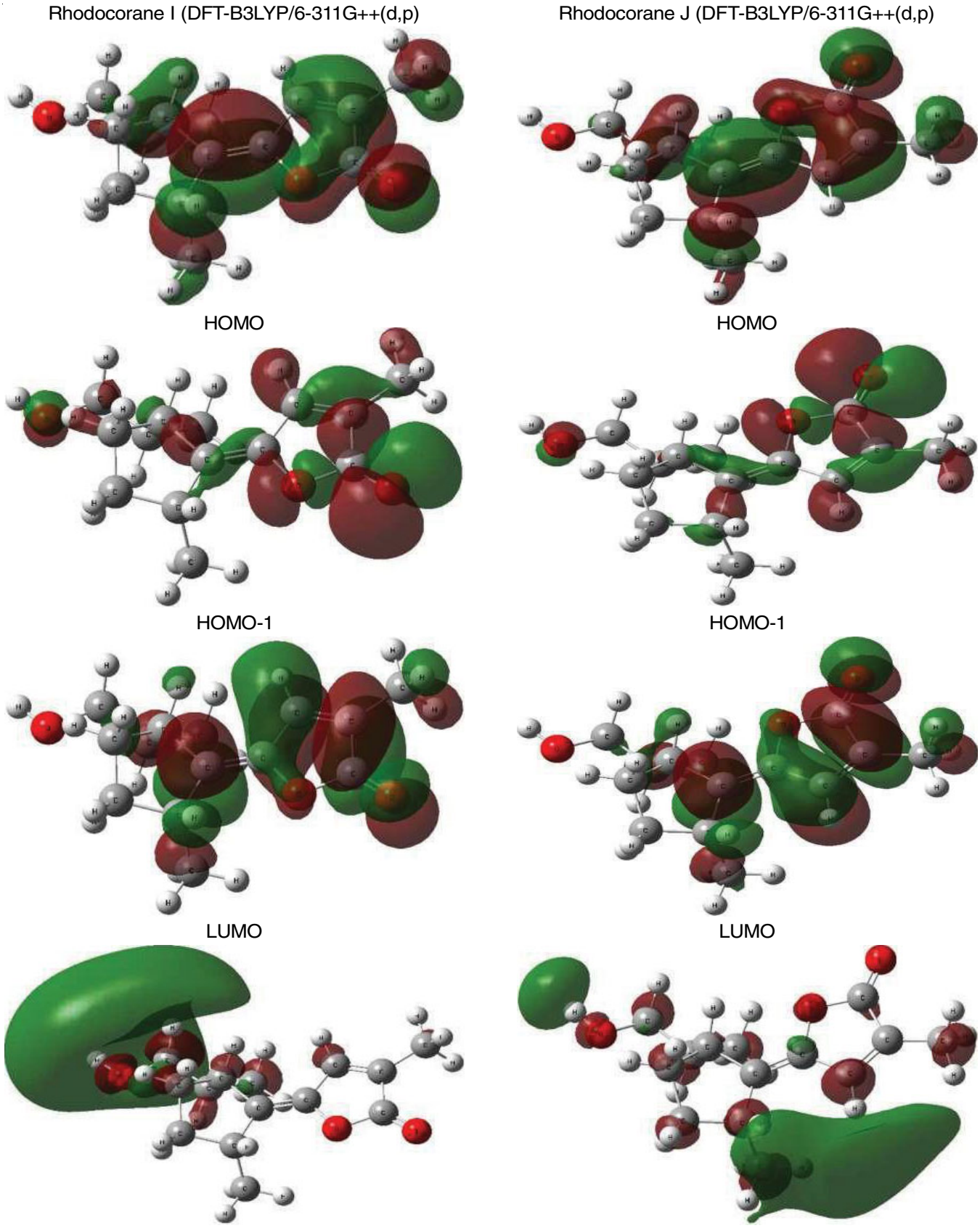

Fig. 2. Molecular orbitals HOMO-LUMOs of Rh-I and Rh-J

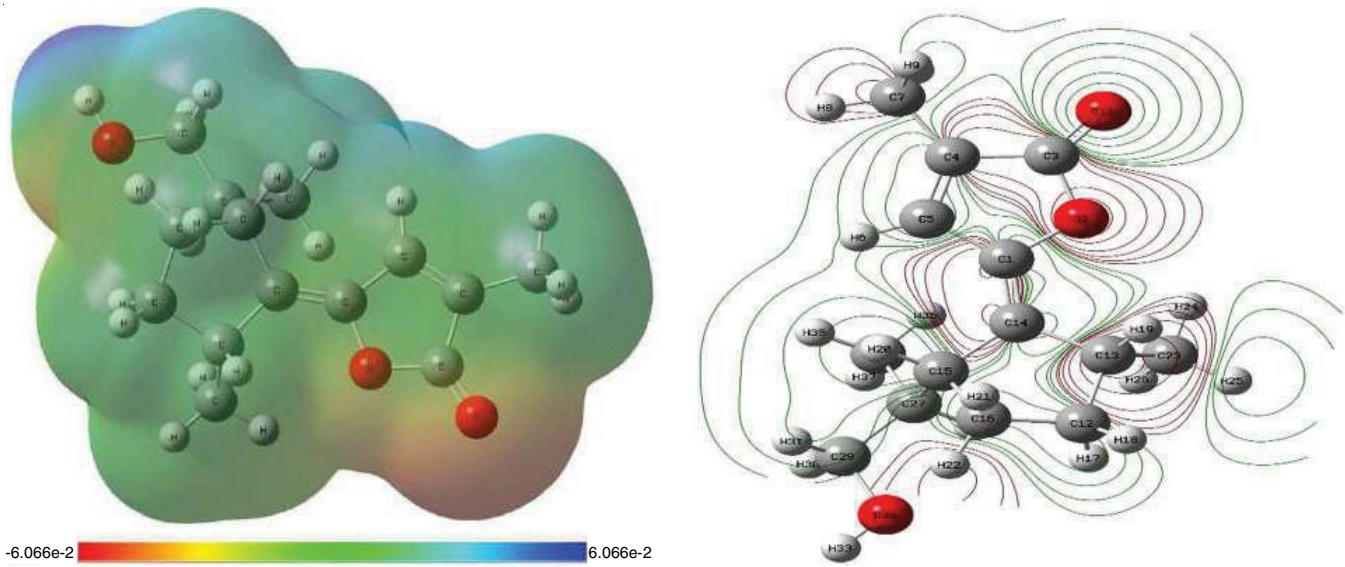

Fig. 3. View of the molecular electrostatic potential surface of the ground state of the optimized structure of rhodocorane

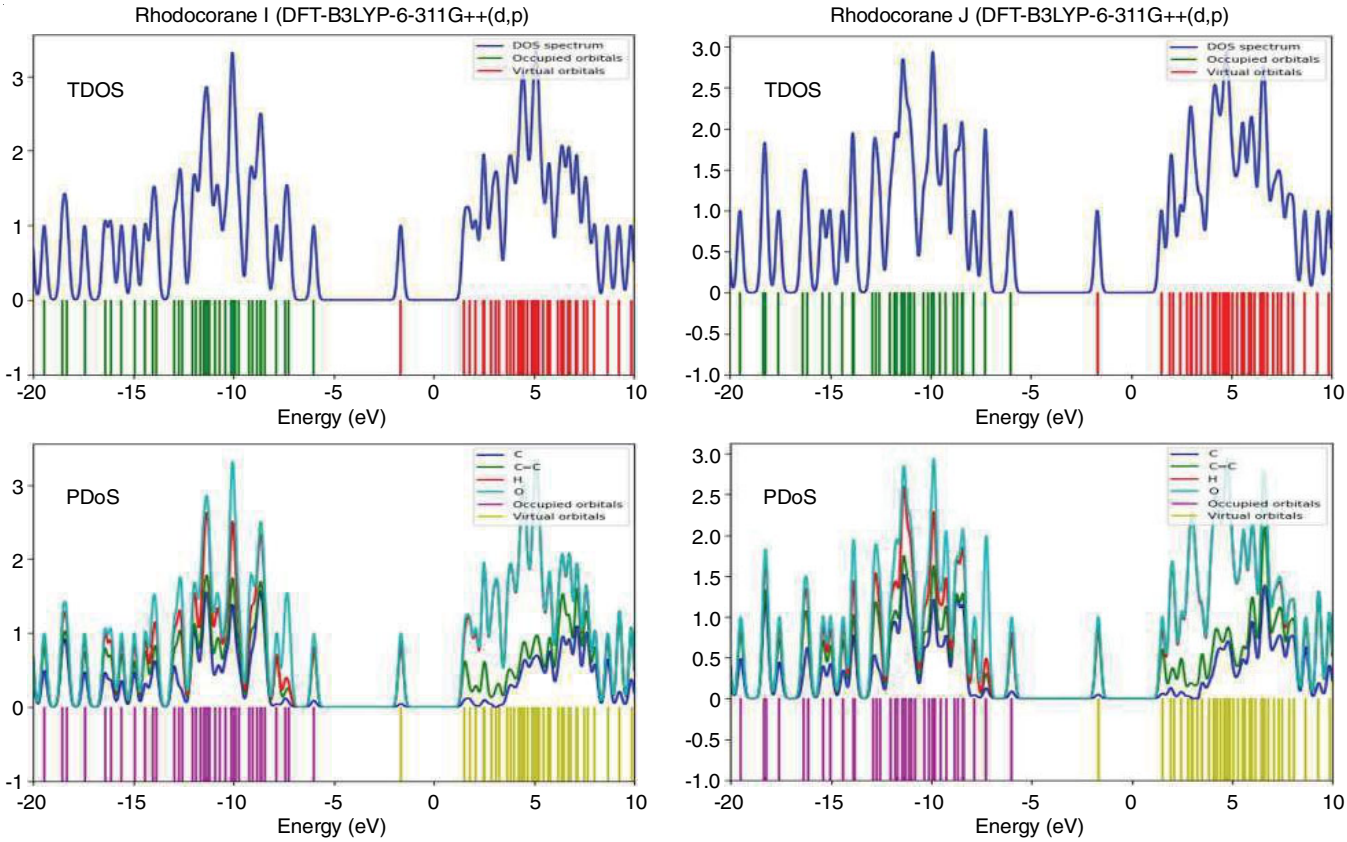

Fig. 4. TDoS and PDoS spectra of Rh-I and Rh-J in gas phase with energy gap

(1.83097 a.u), while LP2(O32) occupies a low energy orbital (0.0028 a.u) with a p-character (99.88%) and a high occupation number (1.9595). Furthermore, it has been observed that the oxygen atoms LP(2) indicates that the bond is purely in p-character, while the σ orbital of O2, O11 and O32 atoms' LP(1) has the %s and %p-characters, indicating that the bond is the hybridized molecular orbital.

Reduced density gradient (RDG): By determining the electron density in the molecular system, Johnson *et al*. [30] developed a framework to explain the weak interactions in real space. The RDG is a dimensionless quantity and initially derived as:

$$RDG(r) = \frac{1}{(3\pi^2)^{1/3}} \frac{|\Delta^2 \rho(r)|}{\rho(r)^{4/3}}$$

The weak interaction is investigated in the region of low electron density. Figs. 5 and 6 show the electron density ρ(RDG) *vs.* multiplied by the sign of λ2. The difference between bonding

TABLE-7
R-I's SECOND ORDER PERTURBATION THEORY ANALYSIS OF FOCK MATRIX IN NBO BASIS

Donor (i)	Type	ED/e	Acceptor (j)	Type	ED/e	E(2)[a] (kcal/mol)	E(j)?E(i)[b] (a.u.)	F(i,j)[c] (a.u.)
C1–C14	π	1.82669	C4–C5	π*	1.83486	14.53	0.32	0.061
C4–C5	π	1.83486	C1–C14	π*	1.82669	16.27	0.34	0.066
C4–C5	π	1.83486	C3–O11	π*	1.97821	21.49	0.3	0.074
C27–C34	σ	1.9788	C12–C16	σ*	1.98261	10.21	1.36	0.105
C27–C34	σ	1.9788	C34–H36	σ*	1.98824	13.01	3.16	0.182
C27–C34	σ	1.9788	C34–H37	σ*	1.98835	32.05	4.12	0.326
C34–H35	σ	1.98838	C34–H35	σ*	1.98838	8.57	3.37	0.152
C34–H35	σ	1.98838	C34–H37	σ*	1.98835	24.61	4.02	0.281
C34–H36	σ	1.98824	C34–H35	σ*	1.98838	16.35	3.37	0.209
C34–H36	σ	1.98824	C34–H36	σ*	1.98824	8.75	3.06	0.146
C34–H36	σ	1.98824	C34–H37	σ*	1.98835	12.11	4.02	0.197
C34–H37	σ	1.98835	C7–H10	σ*	1.97443	11.16	1.07	0.097
C34–H37	σ	1.98835	C12–C16	σ*	1.98261	19.11	1.25	0.138
C34–H37	σ	1.98835	C12–H17	σ*	1.98208	10.86	1.1	0.098
C34–H37	σ	1.98835	C13–C14	σ*	1.96472	11.27	1.13	0.101
C34–H37	σ	1.98835	C15–C27	σ*	1.9623	8.29	0.86	0.076
C34–H37	σ	1.98835	C34–H35	σ*	1.98838	19.94	3.36	0.231
C34–H37	σ	1.98835	C34–H36	σ*	1.98824	12.63	3.05	0.175
C34–H37	σ	1.98835	C34–H37	σ*	1.98835	52.29	4.02	0.41
O2	LP(2)	1.77515	C1–C14	π*	1.82669	22.33	0.38	0.083
O2	LP(2)	1.77515	C3–O11	π*	1.97821	36.36	0.34	0.101
O11	LP(2)	1.83097	O2–C3	σ*	1.98967	36.39	0.58	0.131
O11	LP(2)	1.83097	C3–C4	σ*	1.97224	17.11	0.7	0.1
C3–O11	π	1.97821	C4–C5	π*	1.83486	69.49	0.02	0.072
C4–C5	π	1.83486	C1–C14	π*	1.82669	59	0.01	0.064

[a]$E^{(2)}$ means energy of hyper conjugative interaction (stabilization energy); [b]Energy difference between donor and acceptor i and j NBO orbitals; [c]F(i,j) is the Fork matrix element between i and j NBO orbitals

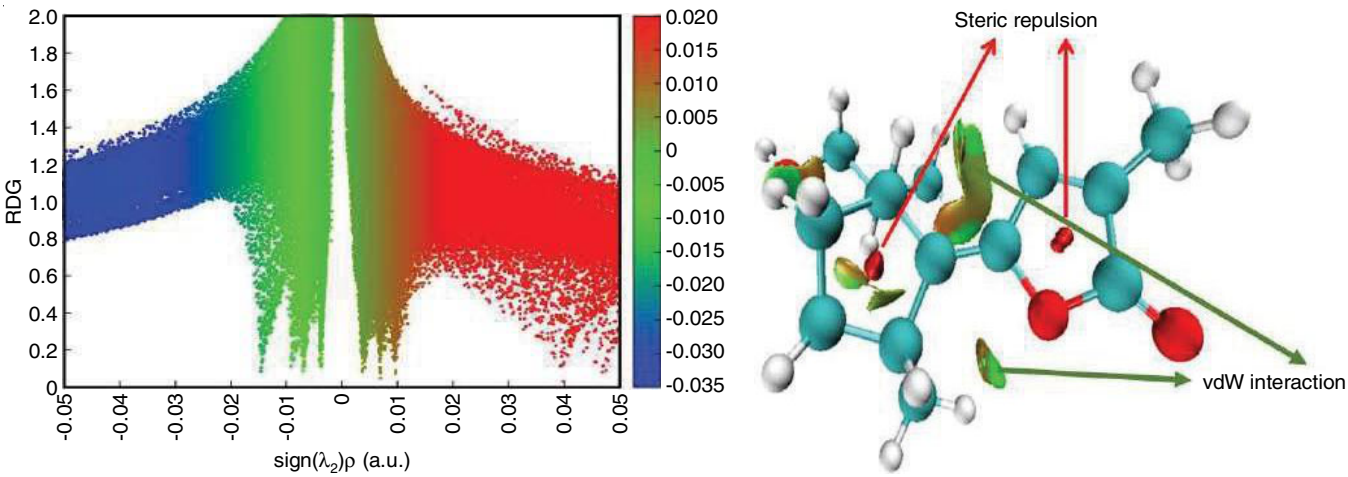

Fig. 5. The reduced density gradient (a) and colour (blue-green scale) surface (b) of R-I according to λ2

(λ2 < 0) and non-bonding (λ2 > 0) is aided by the factor λ2. The VMD program and the Multiwfn program are used to compute the RDG. The molecule possesses an attraction and repulsion spike, as indicated by the RDG 0.10 lines on the RDG diagram. A negative value of (λ2) ρ indicates strong attraction, while a positive value of the sign indicates strong repulsion. The evaluation reveals extremely weak van der Waals (VdW) interactions. The colour red to blue indicates stronger to repulsive interactions in the molecular system. The green interaction region clearly shows that the molecule has a VdW interaction. This interaction occurs between the O in the furanone ring and the H's in the methyl group as a result of hydrogen bonding with the bond lengths 2.68 (O2-H24) and 2.72 (O2-H24). The oxygen atom exhibits a strong steric effect in the title molecule's ring, which is indicated by its red colour.

The electron pair in the molecule is located using ELF, which likewise has a scalar function η(r) and is connected to the Fermi hole curvature. Because of Pauli relation, it calculates

TABLE-8
NBO RESULT SHOWING THE FORMATION OF LEWIS AND NON-LEWIS ORBITALS FOR RHODOCORANE I (DFT-B3LYP-6-311G++(d,p) METHOD

Bond (A-B)	ED/Energy (a.u.)	EDA (%)	EDB (%)	NBO	S (%)	P (%)
σ(C1-O2)	1.98505/0.0236	31.81	68.19	0.5640 ($sp^{3.61}$)C + 0.8258 ($sp^{2.2}$)O	21.66/31.19	78.09/68.74
σ*(C1-O2)	0.03542/0.0236	68.19	31.81	0.8258 ($sp^{3.61}$)C + -0.5640 ($sp^{2.2}$)O	21.66/31.19	78.09/68.74
σ(C1-C5)	1.97046/-0.0099	50.64	49.36	0.7116 ($sp^{1.9}$)C + 0.7025 ($sp^{2.21}$)C	34.47/31.1	65.49/68.84
σ*(C1-C5)	0.03228/0.0099	49.36	50.64	0.7025 ($sp^{1.9}$)C + -0.7116 ($sp^{2.21}$)C	34.47/31.1	65.49/68.84
σ(C1-C14)	1.97766/-0.0092	50.97	49.03	0.7139 ($sp^{1.29}$)C + 0.7002 ($sp^{1.67}$)C	43.75/37.47	56.23/62.47
σ*(C1-C14)	0.0249/0.0092	49.03	50.97	0.7002 ($sp^{1.29}$)C + -0.7139 ($sp^{1.67}$)C	43.75/37.47	56.23/62.47
π(C1-C14)	1.82669/-0.0029	52.69	47.31	0.7258 ($sp^{99.99}$)C + 0.6879 ($sp^{1.00}$)C	0.02/0.01	99.94/99.92
π*(C1-C14)	0.17549/0.0029	47.31	52.69	0.6879 ($sp^{99.99}$)C + -0.7258 ($sp^{1.00}$)C	0.02/0.01	99.94/99.92
σ(O2-C3)	1.98967/-0.0138	69.36	30.64	0.8328 ($sp^{2.51}$)O + 0.5535 ($sp^{2.90}$)C	28.51/25.6	71.42/74.12
σ*(O2-C3)	0.11533/0.0138	30.64	69.36	0.5535 ($sp^{2.51}$)O + -0.8328 ($sp^{2.90}$)C	28.51/25.6	71.42/74.12
σ(C3-C4)	1.97224/-0.0019	48.65	51.35	0.6975 ($sp^{1.53}$)C + 0.7166 ($sp^{2.65}$)C	39.43/27.4	60.51/72.53
σ*(C3-C4)	0.07393/0.0019	51.35	48.65	0.7166 ($sp^{1.53}$)C + -0.6975 ($sp^{2.65}$)C	39.43/27.4	60.51/72.53
σ(C3-O11)	1.99506/-0.0161	35.33	64.67	0.5944 ($sp^{1.87}$)C + 0.8042 ($sp^{1.40}$)O	34.76/41.53	65.09/58.34
σ*(C3-O11)	0.01292/-0.0161	64.67	35.33	0.8042 ($sp^{1.87}$)C + -0.5944 ($sp^{1.40}$)O	34.76/41.53	65.09/58.34
π(C3-O11)	1.97821/0.0201	30.87	69.13	0.5556 ($sp^{1.00}$)C + 0.8314 ($sp^{1.00}$)O	0/0	99.56/99.87
π*(C3-O11)	0.27447/0.0201	69.13	30.87	0.8314 ($sp^{1.00}$)C + -0.5556 ($sp^{1.00}$)O	0/0	99.56/99.87
σ(C4-C5)	1.97471/-0.009	50.42	49.58	0.7101 ($sp^{1.72}$)C + 0.7041 ($sp^{1.72}$)C	36.77/36.73	63.18/63.22
σ*(C4-C5)	0.01708/0.0123	49.58	50.42	0.7041 ($sp^{1.72}$)C + -0.7101 ($sp^{1.72}$)C	36.77/36.73	63.18/63.22
π(C4-C5)	1.83486/0.0096	51.19	48.81	0.7154 ($sp^{1.00}$)C + 0.6987 ($sp^{1.00}$)C	0/0	99.9/99.9
π*(C4-C5)	0.16181/-0.0096	48.81	51.19	0.6987 ($sp^{1.00}$)C + -0.7154 ($sp^{1.00}$)C	0/0	99.9/99.9
σ(C4-C7)	1.98412/-0.0078	51.49	48.51	0.7176 ($sp^{1.79}$)C + 0.6965 ($sp^{2.35}$)C	35.81/29.81	64.17/70.15
σ*(C4-C7)	0.01612/0.0101	48.51	51.49	0.6965 ($sp^{1.79}$)C + -0.7176 ($sp^{2.35}$)C	35.81/29.81	64.17/70.15
σ(C12-C13)	1.97814/-0.0061	48.95	51.05	0.6996 ($sp^{2.71}$)C + 0.7145 ($sp^{2.85}$)C	26.94/25.95	73.02/74.01
σ*(C12-C13)	0.01862/-0.0061	51.05	48.95	0.7145 ($sp^{2.71}$)C + -0.6996 ($sp^{2.85}$)C	26.94/25.95	73.02/74.01
σ(C12-C16)	1.98261/-0.0017	49.98	50.02	0.707 ($sp^{2.69}$)C + 0.7073 ($sp^{2.72}$)C	27.07/26.86	72.89/73.1
σ*(C12-C16)	0.01038/0.0009	50.02	49.98	0.7073 ($sp^{2.69}$)C + -0.707 ($sp^{2.72}$)C	27.07/26.86	72.89/73.1
σ(C13-C14)	1.96472/-0.0096	49.38	50.62	0.7027 ($sp^{2.83}$)C + 0.7115 ($sp^{2.24}$)C	26.12/30.87	73.83/69.1
σ*(C13-C14)	0.02937/-0.0096	50.62	49.38	0.7115 ($sp^{2.83}$) C + -0.7027 ($sp^{2.24}$)C	26.12/30.87	73.83/69.1
σ(C13-C23)	1.9745/0.015	51.83	48.17	0.7199 ($sp^{2.66}$)C + 0.6941 ($sp^{2.42}$)C	27.28/29.24	72.68/70.72
σ*(C13-C23)	0.01519/-0.015	48.17	51.83	0.6941 ($sp^{2.66}$)C + -0.7199 ($sp^{2.42}$)C	27.28/29.24	72.68/70.72
σ(C14-C15)	1.96275/-0.0094	50.12	49.88	0.7079 ($sp^{2.17}$)C + 0.7063 ($sp^{2.83}$)C	31.59/26.08	68.38/73.86
σ*(C14-C15)	0.02526/0.0094	49.88	50.12	0.7063 ($sp^{2.17}$)C + -0.7079 ($sp^{2.83}$)C	31.59/26.08	68.38/73.86
σ(C15-C16)	1.96825/-0.0005	51.59	48.41	0.7183 ($sp^{2.92}$)C + 0.6957 ($sp^{2.77}$)C	25.48/26.51	74.47/73.45
σ*(C15-C16)	0.01807/0.0005	48.41	51.59	0.6957 ($sp^{2.92}$)C + -0.7183 ($sp^{2.77}$)C	25.48/26.51	74.47/73.45
σ(C15-C27)	1.9623/0.0083	50.24	49.76	0.7088 ($sp^{2.77}$)C + 0.7054 ($sp^{2.70}$)C	26.54/26.99	73.42/72.97
σ*(C15-C27)	0.03526/-0.0083	49.76	50.24	0.7054 ($sp^{2.77}$)C + -0.7088 ($sp^{2.70}$)C	26.54/26.99	73.42/72.97
σ(C27-C29)	1.97745/-0.0091	50.59	49.41	0.7113 ($sp^{2.92}$)C + 0.7029 ($sp^{2.24}$)C	25.52/30.86	74.43/69.1
σ*(C27-C29)	0.02253/0.0067	49.41	50.59	0.7029 ($sp^{2.92}$)C + -0.7113 ($sp^{2.24}$)C	25.52/30.86	74.43/69.1
σ(C27-C34)	1.9788/-0.0023	51.22	48.78	0.7157 ($sp^{2.76}$)C + 0.6984 ($sp^{2.39}$)C	26.6/29.46	73.36/70.5
σ*(C27-C34)	0.01025/0.0005	48.78	51.22	0.6984 ($sp^{2.76}$)C + -0.7157 ($sp^{2.39}$)C	26.6/29.46	73.36/70.5
σ(C29-O32)	1.99376/-0.0202	33.07	66.93	0.5751 ($sp^{3.60}$)C + 0.8181 ($sp^{2.37}$)O	21.68/29.67	78.11/70.25
σ*(C29-O32)	0.01412/-0.017	66.93	33.07	0.8181 ($sp^{3.60}$)C + -0.5751 ($sp^{2.37}$)O	21.68/29.67	78.11/70.25
LP1(O2)	1.96922/0.0049			$sp^{1.48}$	40.31	59.66
LP2(O2)	1.77515/0.0084			$sp^{1.00}$	0.00	99.94
LP1(O11)	1.97965/0.0069			$sp^{0.71}$	58.47	41.52
LP2(O11)	1.83097/0.0008			$sp^{99.99}$	0.07	99.85
LP1(O32)	1.98173/0.0047			$sp^{1.00}$	49.90	50.07
LP2(O32)	1.9595/0.0028			$sp^{99.99}$	0.08	99.88

extra kinetic energy density. Fig. 7 displays a 3D plot of the ELF with the following colours: orange regions indicate charge, whereas blue regions indicate charge depletion and green area indicates the weak interaction of a molecule. The carbon atoms exhibit charge depletion at rhodocorane-I and between the orange is used to symbolize the accumulation of two carbon atom charges.

Drug likeness: The compound rhodocorane have been examined for its potential to play a crucial part in the pharmaceutical products by looking at its drug similarity parameter. The hypothesized values of hydrogen bond donors (HBD), hydrogen bond acceptors (HBA), number of rotatable bonds, Alog P, polar surface area (PSA) and molar refractivity for the rhodocorane molecule are shown in Table-9, which summ-

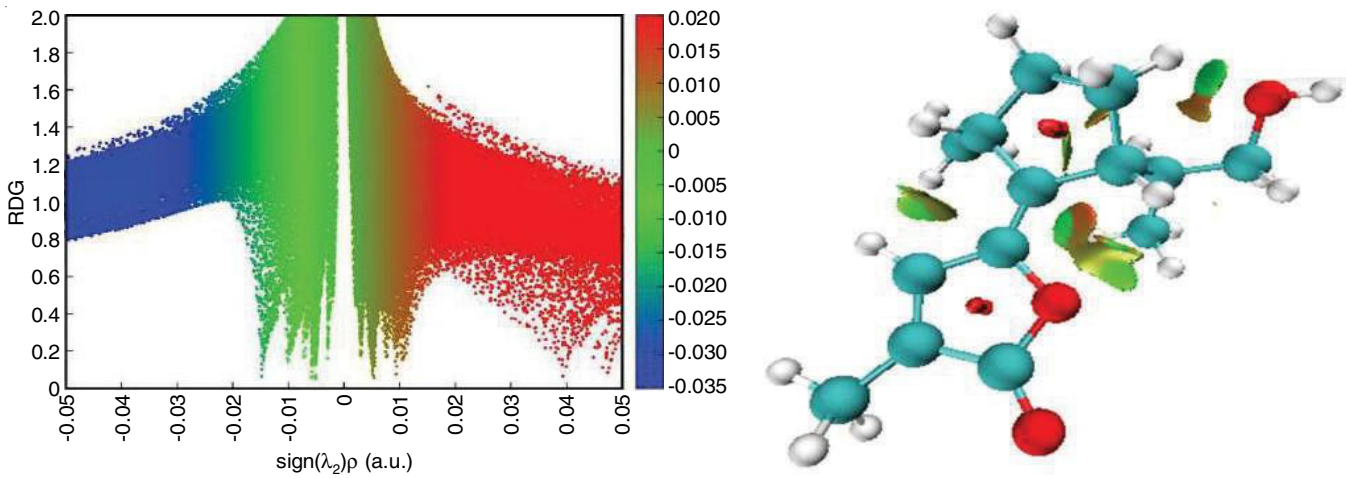

Fig. 6. The reduced density gradient (a) and colour (blue-green scale) surface (b) of R-J according to λ2

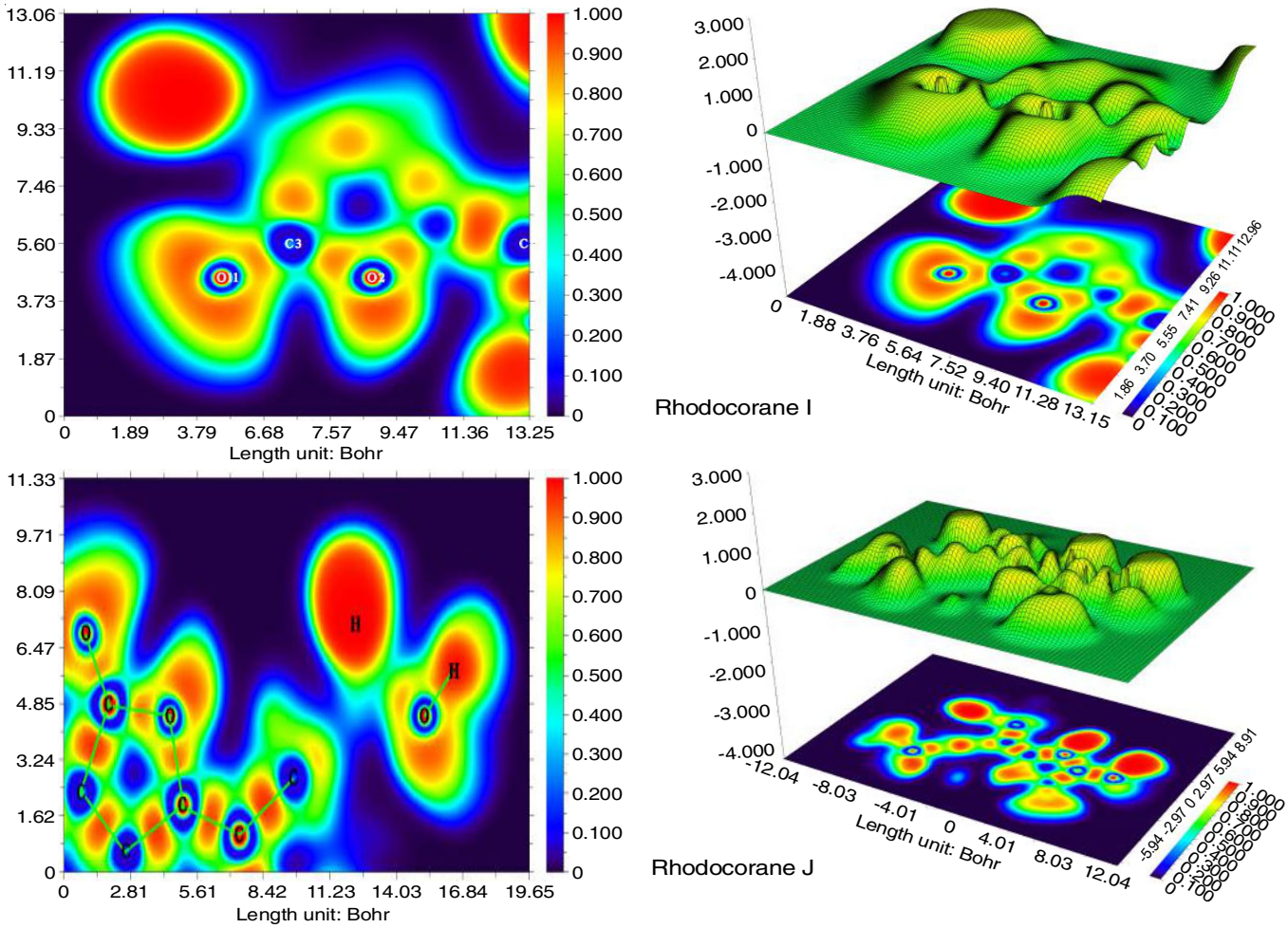

Fig. 7. 3D Electron localization function diagram of rhodocorane-I and rhodocorane-J

arizes the drug similarity parameters. The rotatable bond in the molecule is permitted if it is within the range of HBD and HBA, which are fewer than 5 and 10, respectively, in accordance with Lipinski's rule of five [31]. According to Lipinski's rule of five, the molecule's hydrophobic/lipophilic nature is indicated by an Alog P value which is less than 5. Three hydrogen bond acceptors, an Alog P value of 2.21 and a molecular refractive index of 66.68 lie within the specified 40-130 permitted range for the pharmaceutical drugs [32,33] title compound has been regarded as a pharmaceutical active molecule based on the findings mentioned above.

Rhodocorane is preferred in all the six criteria taken into consideration and is linked to a fourth class of toxicity, according to the SwissADME [34-36] bioavailability radar and Pro-

TABLE-9
FREQUENCY CONSIDERED DRUG
LIKENESS PARAMETERS CALCULATED

Descriptor	Value
Number of hydrogen bond acceptor	3
Number of hydrogen bond donor	1
Alog P	2.42
Molecular weight (g/mol)	236.31 g/mol
Molar refractivity	66.68
Number of rotatable bonds	2
Topological polar surface area (Å^2)	46.53 Å
Number of heavy atoms	0

Tox-II [37,38] (Fig. 8). Furthermore, the BOILED-Egg method, which is based on the lipohilicity and polarity, is one of the effective ways to evaluate compounds for human blood-brain barrier (BBB) penetration and gastrointestinal absorption (GIA). Therefore, the compounds that were projected to passively pass through the blood-brain barrier and passively be absorbed by the gastrointestinal tract are represented by spots in the yolk and white of the egg, respectively. Furthermore, the P-glycoprotein displays blue dots for molecules that are effluated (PGP+) and red dots for molecules that are not effluated (PGP–) from the central nervous system. Pyridoxal was therefore expected

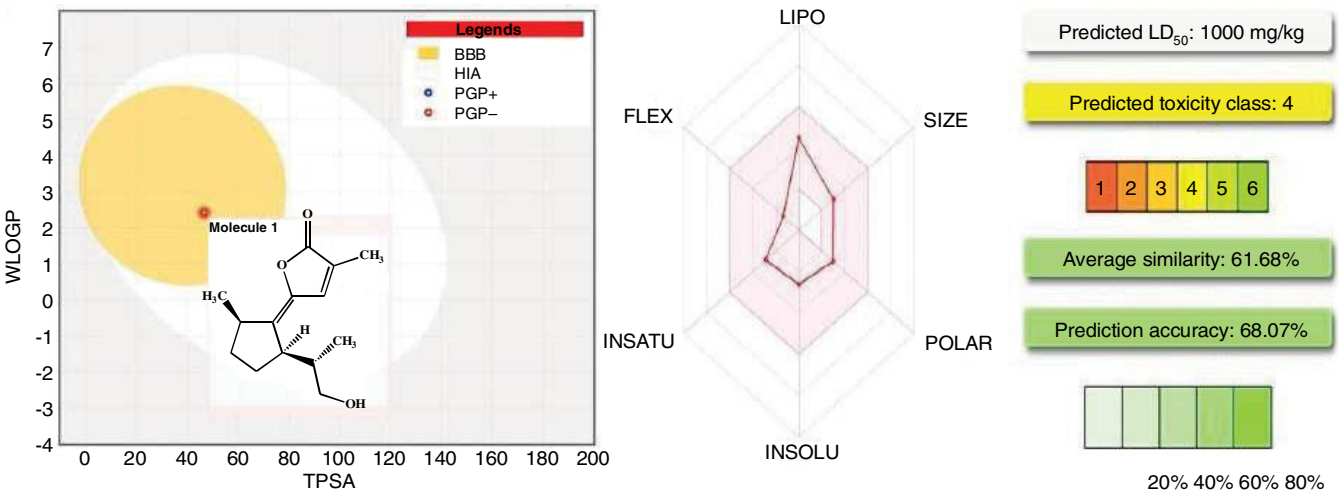

TOXICITY MODEL REPORTS

Classification	Target	Shorthand	Prediction	Probability
Organ toxicity	Hepatotoxicity	dili	Inactive	0.75
Organ toxicity	Neurotoxicity	neuro	Inactive	0.82
Organ toxicity	Respiratory toxicity	respi	Inactive	0.61
Organ toxicity	Cardiotoxicity	cardio	Inactive	0.73
Toxicity end points	Carcinogenicity	carcino	Inactive	0.63
Toxicity end points	Immunotoxicity	immuno	Inactive	0.70
Toxicity end points	Mutagenicity	mutagen	Inactive	0.87
Toxicity end points	Cytotoxicity	cyto	Inactive	0.82
Toxicity end points	Ecotoxicity	eco	Inactive	0.56
Toxicity end points	Clinical toxicity	clinical	Inactive	0.63
Toxicity end points	Nutritional toxicity	nutri	Inactive	0.58
Tox21-Nuclear receptor signalling pathways	Aryl hydrocarbon Receptor (AhR)	nr_ahr	Inactive	0.82
Tox21-Nuclear receptor signalling pathways	Androgen Receptor (AR)	nr_ar	Inactive	0.95
Tox21-Nuclear receptor signalling pathways	Androgen Receptor Ligand Binding Domain (AR-LBD)	nr_ar_lbd	Inactive	0.97
Tox21-Nuclear receptor signalling pathways	Aromatase	nr_aromatase	Inactive	0.84
Tox21-Nuclear receptor signalling pathways	Estrogen Receptor Alpha (ER)	nr_er	Inactive	0.89
Tox21-Nuclear receptor signalling pathways	Estrogen Receptor Ligand Binding Domain (ER-LBD)	nr_er_lbd	Inactive	0.97
Tox21-Nuclear receptor signalling pathways	Peroxisome Proliferator Activated Receptor Gamma (PPAR-Gamma)	nr_ppar_gamma	Inactive	0.85
Tox21-Stress response pathways	Nuclear factor (erythroid-derived 2)-like 2/antioxidant responsive element (nrf2/ARE)	sr_are	Inactive	0.90
Tox21-Stress response pathways	Heat shock factor response element (HSE)	sr_hse	Inactive	0.90
Tox21-Stress response pathways	Mitochondrial Membrane Potential (MMP)	sr_mmp	Inactive	0.86
Tox21-Stress response pathways	Phosphoprotein (Tumor Supressor) p53	sr_p53	Inactive	0.91
Tox21-Stress response pathways	ATPase family AAA domain-containing protein 5 (ATAD5)	sr_atad5	Inactive	0.98

Fig. 8. BOILED-Egg model (top-left), the bioavailability radar (the coloured zone of the radar is the suitable physico-chemical space for oral bioavailability of rhododcorane) within the domain boarders of ADME properties, calculated by SWISSADME (topmiddle) and toxicity results, calculated by Pro-Tox-II (top-right and bottom), of rhodocorane

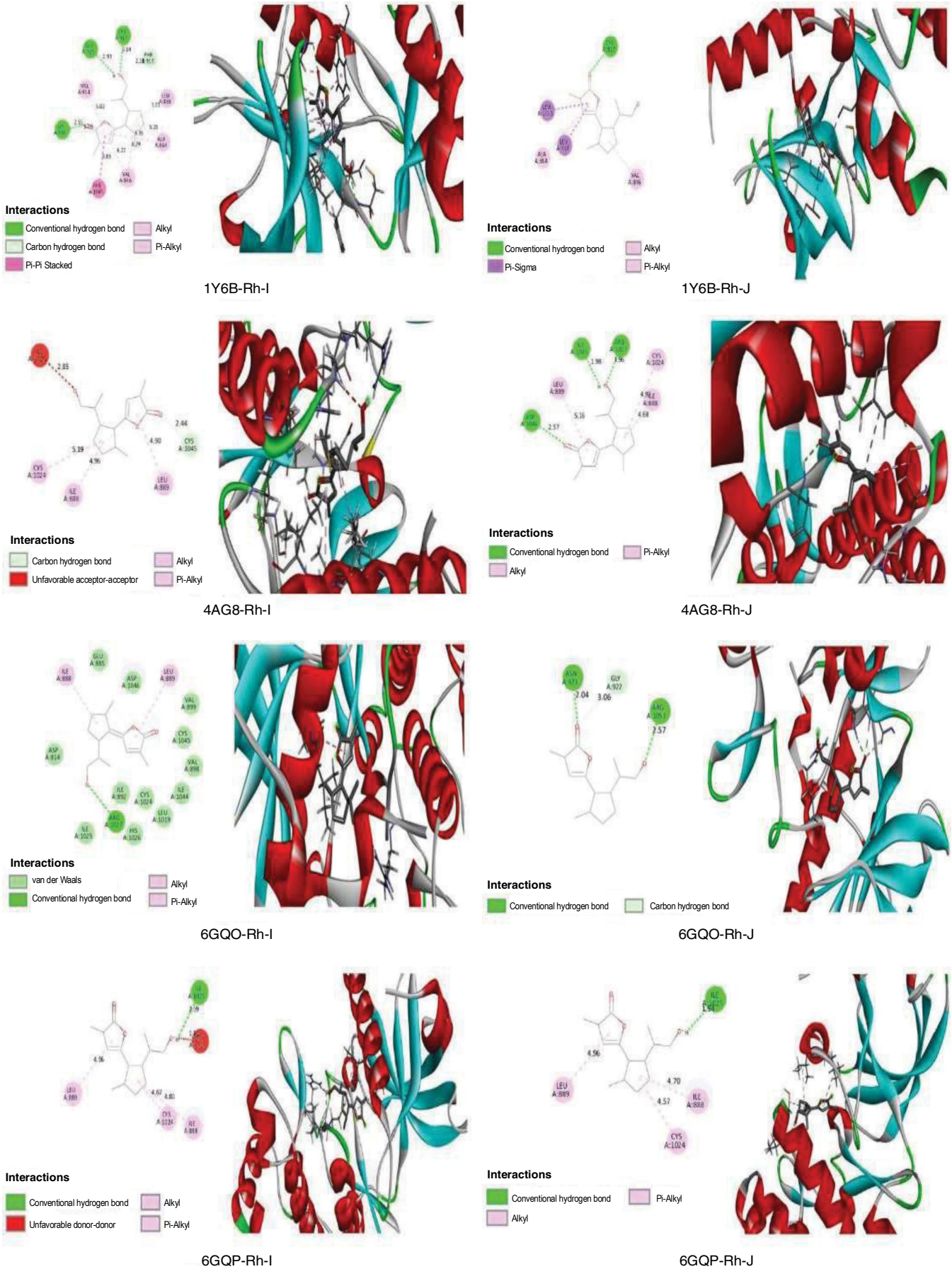

Fig. 9. Docking and hydrogen bond interactions of Rh-I and Rh-J with 1Y6B, 4AG8 6GQO and 6GQP

to have a favourable GIA property with the PGP-effect and a negative BBB penetration. Furthermore, Rh-I was found to be non-totoxic as shown by the toxicity model report (Fig. 8).

Molecular docking: VEGFR2 kinase receptor proteins with PDB IDs (1Y6B, 4AG8 6GQO and 6GQP) were taken for docking from the protein data bank in order to perform the molecular docking studies. UCSF-chimera 1.18 and Discovery Studio were utilized to open the optimized ligand structures and saved in .sdf format. Following the addition of hydrogen and the assignment of Gasteiger charges, ligand and protein were prepared using UCSF-chimera, followed by the energy minimization. Auto-grid, which was assigned to the macromolecule center, was used to generate the grid box. After that, the grid box was resized to encompass the entire protein. AutoDock Vina was used for docking and Biovia Discovery Studio v24.1.0.23298 was used to visualize the results after they were saved as .pdbqt and the results are summarized in Table-10.

TABLE-10
MOLECULAR DOCKING AND HYDROGEN BOND

PDB code	Docking score (Kcal/mol)	
	Rh-I	Rh-J
1Y6B	-7.1	-6.9
4AG8	-7.1	-6.8
6GQO	-6.77	-6.74
6GQP	-6.4	-6.2

VEGFR2 is crucial for promoting tumour angiogenesis and outgrowth in tumours. Indeed, it is frequently discovered that VEGFR2 and its family members are dysregulated and overexpressed in a variety of cancer types, including breast, colon and lung cancers [39]. The compound with the highest docking score, Rh-I, demonstrated a good binding interaction with the VEGFR2 kinase receptor's 1Y6B and 4AG8 backbone. Hydrogen bonds with GLU915, CYS917 and LYS866 are developed when Rh-I interacts with 1Y6B. However, 4AG8 demonstrated H-bonding with Rh-J, which had bonds with the amino acids ASP1046, ARG1027 and ILE1025. Apart from the H-bonding, both moieties exhibit π-alkyl interactions, while Rh-I exhibited π-π stacking interaction with PHE1045 of 1Y6B (Fig. 9).

Conclusion

The structural, vibrational, NMR, electronic and reactivity aspects of rhodocorane I and J were thoroughly examined using the density functional theory B3LYP/6-311G++(d,p) method. The outcomes were also compared with the experimental values. Using the DFT calculations and a quantum chemical approach, a thorough vibrational dynamical and molecular structure analysis of rhodocoranes has been accomplished. For the first time, spectral characterization investigations, including FT-IR and NMR for Rh-I & J, have been conducted. The delocalization in the furanone ring is reflected in the NBO result and the associated stabilization energies are given. The furanone and cyclopentyl rings were found to exhibit steric repulsion, according to the reduced density gradient (RDG) analysis. Moreover, it is demonstrated that the moieties within molecules had H-bonding and van der Waals interactions. In addition to predicting primarily the $\pi \rightarrow \pi^*$ type electronic transitions, which are of the intramolecular charge transfer type, the experimental and theoretical UV-Vis spectral analysis has also shed light on the excitation energy and oscillator strength. The MEP map indicates that the alcohol group and the oxygen atoms of the furanone ring have negative potential sites, while the hydrogen atoms of the C–H in the cyclopentyl ring have positive potential sites. The results of the ADME and toxicity studies indicated that both isomers complied with the Lipinski rule of five and the compound in question was deemed non-toxic and a pharmaceutical active molecule. VEGFR2 kinase receptor proteins (Homosapiens) have been subjected to the molecular docking studies with the isomers Rh-I and J. With the receptor that causes cancer, the proteins displayed a good docking score. Understanding the characteristics and activity of Rh-I and J may result from the current quantum chemical investigation, which may also facilitate the use of these elements in more sophisticated applications. Thus, it is anticipated that the results will help in the search for the experimental and theoretical evidences supporting the title chemical, which could lead to the development of novel pharmaceuticals.

ACKNOWLEDGEMENTS

One of the authors, JPC acknowledges the financial support from Council of Scientific and Industrial Research (CSIR-JRF), for support of this work File No. 08/0603(13662)/2022-EMR-I.

CONFLICT OF INTEREST

The authors declare that there is no conflict of interests regarding the publication of this article.

REFERENCES

1. K. Kumar, R. Mehra, R.P.F. Guiné, M.J. Lima, N. Kumar, R. Kaushik, N. Ahmed, A.N. Yadav and H. Kumar, *Foods*, **10**, 2996 (2021); https://doi.org/10.3390/foods10122996
2. A. Podkowa, A. Kryczyk-Poprawa, W. Opoka and B. Muszynska, *Eur. Food Res. Technol.*, **247**, 513 (2021); https://doi.org/10.1007/s00217-020-03646-1
3. D. Yadav and P.S. Negi, *Food Res. Int.*, **148**, 110599 (2021); https://doi.org/10.1016/j.foodres.2021.110599
4. B. Sandargo, M. Michehl, D. Praditya, E.Steinmann, M. Stadler and F. Surup, *Org. Lett.*, **21**, 3286 (2019); https://doi.org/10.1021/acs.orglett.9b01017
5. B. Sandargo, M. Michehl, M. Stadler and F. Surup, *J. Nat. Prod.*, **83**, 720 (2020); https://doi.org/10.1021/acs.jnatprod.9b00871
6. K. Kumar, R. Mehra, R.P.F. Guiné, M.J. Lima, N. Kumar, R. Kaushik, N. Ahmed, A.N. Yadav and H. Kumar, *Foods*, **10**, 2996 (2021); https://doi.org/10.3390/foods10122996
7. N.K. Fuloria, R.K. Raheja, K.H. Shah, M.J. Oza, Y.A. Kulkarni, V. Subramaniyan, M. Sekar and S. Fuloria, *Front. Pharmacol.*, **13**, 830103 (2022); https://doi.org/10.3389/fphar.2022.830103
8. S.A. Heleno, L. Barros, A. Martins, M.J.R.P. Queiroz, C. Santos-Buelga and I.C.F.R. Ferreira, *J. Agric. Food Chem.*, **60**, 4634 (2012); https://doi.org/10.1021/jf300739m
9. M. Zhao, Y. Tang, J. Xie, Z. Zhao and H. Cui, *Eur. J. Med. Chem.*, **209**, 112860 (2021); https://doi.org/10.1016/j.ejmech.2020.112860
10. W.C. Sum, S.S. Ebada, J. Clement Matasyoh and M. Stadler, *Curr. Res. Biotechnol.*, **6**, 100155 (2023); https://doi.org/10.1016/j.crbiot.2023.100155

11. C.A. Vincent, V.N. Nair and U.K. Tambar, *Org. Lett.*, **26**, 8453 (2024); https://doi.org/10.1021/acs.orglett.4c02764
12. M.J. Frisch, G.W. Trucks, H.B. Schlegel, G.E. Scuseria, M.A. Robb, J.R. Cheeseman, G. Scalmani, V. Barone, G.A. Petersson, H. Nakatsuji, X. Li, M. Caricato, A. Marenich, J. Bloino, B.G. Janesko, R. Gomperts, B. Mennucci, H.P. Hratchian, J.V. Ortiz, A.F. Izmaylov, J.L. Sonnenberg, D. Williams-Young, F. Ding, F. Lipparini, F. Egidi, J. Goings, B. Peng, A. Petrone, T. Henderson, D. Ranasinghe, V.G. Zakrzewski, J. Gao, N. Rega, G. Zheng, W. Liang, M. Hada, M. Ehara, K. Toyota, R. Fukuda, J. Hasegawa, M. Ishida, T. Nakajima, Y. Honda, O. Kitao, H. Nakai, T. Vreven, K. Throssell, J.A. Montgomery, Jr., J.E. Peralta, F. Ogliaro, M. Bearpark, J.J. Heyd, E. Brothers, K.N. Kudin, V.N. Staroverov, T. Keith, R. Kobayashi, J. Normand, K. Raghavachari, A. Rendell, J.C. Burant, S.S. Iyengar, J. Tomasi, M. Cossi, J.M. Millam, M. Klene, C. Adamo, R. Cammi, J. W. Ochterski, R.L. Martin, K. Morokuma, O. Farkas, J.B. Foresman, and D.J. Fox, Gaussian, Inc., Wallingford CT, Gaussian 09, Revision A.02 (2016).
13. M.H. Jamróz, *Biomol. Spectrosc.*, **114**, 220 (2013); https://doi.org/10.1016/j.saa.2013.05.096
14. T. Lu and F. Chen, *J. Comput. Chem.*, **33**, 580 (2012); https://doi.org/10.1002/jcc.22885
15. E.D. Glendening, C.R. Landis and F. Weinhold, *J. Comput. Chem.*, **34**, 1429 (2013); https://doi.org/10.1002/jcc.23266
16. R. Dltchfield, *J. Chem. Phys.*, **56**, 5688 (1972); https://doi.org/10.1063/1.1677088
17. K. Wolinski, J.F. Hinton and P. Pulay, *J. Am. Chem. Soc.*, **112**, 8251 (1990); https://doi.org/10.1021/ja00179a005
18. E. Cancès, B. Mennucci and J. Tomasi, *J. Chem. Phys.*, **107**, 3032 (1997); https://doi.org/10.1063/1.474659
19. N.M. O'boyle, A.L. Tenderholt and K.M. Langner, *J. Comput. Chem.*, **29**, 839 (2007); https://doi.org/10.1002/jcc.20823
20. W. Humphrey, A. Dalke and K. Schulten, *J. Mol. Graph.*, **14**, 33 (1995); https://doi.org/10.1016/0263-7855(96)00018-5
21. J. Eberhardt, D. Santos-Martins, A.F. Tillack and S. Forli, *J. Chem. Inf. Model.*, **61**, 3891 (2021); https://doi.org/10.1021/acs.jcim.1c00203
22. A. O. Olegtrott, *Softw. News Updat.*, **31**, 455 (2009); https://doi.org/10.1002/jcc.21334
23. E.F. Pettersen, T.D. Goddard, C.C. Huang, G.S. Couch, D.M. Greenblatt, E.C. Meng and T.E. Ferrin, *J. Comput. Chem.*, **25**, 1605 (2004); https://doi.org/10.1002/jcc.20084
24. BIOVIA, Dassault Systèmes, BIOVIA Discovery Studio Visualiser: 2021, San Diego: Dassault Systèmes (2021).
25. L. Vrielynck, J.P. Cornard, J.C. Merlin and M.F. Lautie, *Spectroscopy*, **50**, 2177 (1994); https://doi.org/10.1016/0584-8539(93)E0033-S
26. D.L. Pavia, G.M. Lampman, G.S. Kriz and J.R. Vyvyan, Introduction to Spectroscopy, Brooks/Cole, Cengage Learning, edn. 4 (2001).
27. R. Parthasarathi, J. Padmanabhan, M. Elango, V. Subramanian and P.K. Chattaraj, *Chem. Phys. Lett.*, **394**, 225 (2004); https://doi.org/10.1016/j.cplett.2004.07.002
28. P. Rajesh, S. Gunasekaran and A. Manikandan, *J. Mol. Struct.*, **1144**, 379 (2017); https://doi.org/10.1016/j.molstruc.2017.04.116
29. K.A. Ford, *Mol. Pharm.*, **10**, 1171 (2013); https://doi.org/10.1021/mp3004385
30. E.R. Johnson, S. Keinan, P. Mori-Sánchez, J. Contreras-García, A.J. Cohen and W. Yang, *J. Am. Chem. Soc.*, **132**, 6498 (2010); https://doi.org/10.1021/ja100936w
31. C.A. Lipinski, *Drug Discov. Today. Technol.*, **1**, 337 (2004); https://doi.org/10.1016/j.ddtec.2004.11.007
32. C. A. Lipinski, F. Lombardo, B. W. Dominy, and P. J. Feeney, *Adv. Drug Deliv. Rev.*, **64**, 4 (2012); https://doi.org/10.1016/j.addr.2012.09.019
33. A.K. Ghose, V.N. Viswanadhan and J.J. Wendoloski, *J. Comb. Chem.*, **1**, 55 (1999); https://doi.org/10.1021/cc9800071
34. A. Daina, O. Michielin and V. Zoete, *Sci. Rep.*, **7**, 1 (2017); https://doi.org/10.1038/srep42717
35. A. Daina, O. Michielin and V. Zoete, *Sci. Rep.*, **7**, 42717 (2017); https://doi.org/10.1038/srep42717
36. A. Daina and V. Zoete, *ChemMedChem*, **11**, 1117 (2016); https://doi.org/10.1002/cmdc.201600182
37. P. Banerjee, A.O. Eckert, A.K. Schrey and R. Preissner, *Nucleic Acids Res.*, **46(no. W1)**, W257 (2018); https://doi.org/10.1093/nar/gky318
38. P. Banerjee, A.O. Eckert, A.K. Schrey and R. Preissner, Nucleic Acids Res., **46(Web Server issue),** W257 (2018); https://doi.org/10.1093/nar/gky318
39. P. Celec and Y. Yonemitsu, *Pathophysiology*, **11**, 69 (2004); https://doi.org/10.1016/j.pathophys.2004.03.002